Arabian Journal of Chemistry (2023) **16**, 104413

King Saud University

Arabian Journal of Chemistry

www.ksu.edu.sa
www.sciencedirect.com

ORIGINAL ARTICLE

An approach utilizing the Response Surface Methodology (RSM) to optimize Adsorption-Desorption of Natural Saudi Arabian Diatomite-with the Box- Behnken Design Technique

Murad Alsawalha

Industrial Chemistry Division, Chemical Engineering Department, Jubail Industrial College, P.O. Box: 10099, Jubail City 31961, Saudi Arabia

Received 6 August 2022; accepted 7 November 2022
Available online 12 November 2022

KEYWORDS

Saudi Diatomaceous Earth;
Adsorption-Desorption design;
Catalysts;
Physical properties;
Design optimality;
Dispersion graphs

Abstract Saudi Arabian's natural diatomite samples were subjected to physical adsorption–desorption characterizations using Brunauer-Emmet-Teller (BET) and the Barrett-Joyner-Halenda (BJH), performed under heating of 140 °C for different periods of hours: 6, 12, 18, and 24 h, to create a central optimization design with surface areas and total pore distributions. Seventeen experimental runs resulted in the primary composite factor design. The surface response describes 100 % variability with a determination coefficient of 1, signifying the quadratic model with an expected correlation coefficient (R^2) is satisfied with a standard deviation of 0.2322, demonstrating the high predictability of the model. Moreover, the RSM results have been validated using the *t*-test with the observed R^2 value and adjusted R^2. The model selected with higher F and p values showed < 0.0001, which subsequently described the significance of the developed model. The independent components were explained with the help of 3D surface and contour plots that compare the heating time, elapsed time, pressure, and relative pressure against the dependent variable. The plots revealed that the adsorbed quantities well depended on heating time, elapsed time, pressure, relative pressure for isotherm, BET surface area, Langmuir surface area, and *t*-plot Micropore area.

1. Introduction

Fossilized diatomite deposits are abundant on earth. They are microalgae found in various habitats on land, rivers, or the sea. Diatomite is any sedimentary deposit high in diatomite remains or diatomite silica (hydrated silicon dioxide). Diatomite deposits are both ancient and recent. It can be recognized as crumbly, grey-coloured sediment with a low specific density in dry conditions.

E-mail address: murad_s@rcjy.edu.sa
Peer review under responsibility of King Saud University.

Production and hosting by Elsevier

https://doi.org/10.1016/j.arabjc.2022.104413

(Zahajská et al., 2020; Akin et al., 2000; Flower, 2013). These algae remain well-preserved in the residue due to their hard silica walls. Diatomites have originally been formed by diatom particles or frustules that are single-celled photosynthetic algae in aquatic environments (Harwood et al., 1999; Battarbee et al., 2002; Rachna and Shanker, 2020). There are three main types of diatoms and more than 1000,000 known species in nature. They are primarily amorphous Silica or silica acid and coated in fibrous pectin. Diatomite surface size varies from 5 mm to 200 mm in a preserved state (Zahajská et al., 2020). Physically, diatoms are classified into two major groups; Centrals (a centric diatom) and Pennales (a pennate diatom). Centrals have a radially symmetrical form, with parts radiating from their center. However, Pennales are bilaterally symmetrical. Both left and right parts mirror each other's structure (Zahajská et al., 2020; Flower, 2013).

1.1. General characteristics and extraction of diatomite

Diatomites are abundant worldwide, easy to obtain, and cheap to manufacture. They are also biocompatible and safe to handle. Their characteristic thermal stability and chemical inertia make diatomite a suitable material for producing additives and fillers in manufacturing paints, plastics, rubber, fertilizers (Araújo do Nascimento et al., 2021; Sannikova, 2021), and medical applications (Janićijević et al., 2015; Wei et al., 2022; Huang et al., 2021; Ren et al., 2022; Maher et al., 2018) catalysts (Zhou et al., 2021; Niu et al., 2022; Acharya et al., 2022; Liu et al., 2022; Ghobara et al., 2019; Wang et al., 2013), water treatment (Acharya et al., 2022; Zhang et al., 2022) In its raw extracted form, diatomite (ancient or new) comprises water that includes natural rock (non-biogenic) and organic substances. After extraction and preparation, diatomite with more than 80 % silica becomes commercially valuable. It is sediment composed of 50–80 % silica (Wiemer and Dziadek, 2017). For thousands of years, humans have extracted diatomites, and today, they are used both in the production of industrial products and for geological study. In industry, diatomites are additives and fillers for liquid filtration processes. For example, they can be found in commercial paint manufacturing, rubber products, plastics, pesticides, and fire bricks (Wu and Cong, 2020; Kucuk et al., 2020; Hanif et al., 2022; Elias and Cultrone, 2019). Also, polishes and particular toothpaste contain diatomite due to its lightly abrasive nature. Modern fertilizers on the land have diatomites that stimulate plant growth and development, improve soil quality, and increase plant water absorption. Also, dusting crops with diatomite kills common pests such as aphids, insects, slugs, and snails. The dust also repels insects and pests in grain crop storage silos. (Shen et al., 2021).

Diatomites are lightweight and highly porous. For this reason, they are also widely used in environmental protection in electrical, chemical, and other industries. Additionally, researchers have exploited natural silica nanoparticles in an innovative method as a natural delivery system for treating cancer cells and other diseases (Managò et al., 2021). A study of diatomite earth extracted in Ankara, Turkey, revealed notable changes in the surface areas following the sintering and purification processes (Managò et al., 2021). The investigation comprised three forms of diatomite samples: received, calcined, and purified. This study revealed a significant increase in the specific areas of diatomite samples from 37.5 m^2/g to 81.8 m^2/g. Additionally, a study of sorbent derived from local diatomite modified using aluminum compounds produced changes in the surface areas. (Goren et al., 2002; Wang et al., 2021). Samples were tested employing powder X-ray diffraction, FTIR, differential thermal, adsorption structural (BET), and chemical analyses. Heated diatomite in solutions of NaOH followed by aluminum salt and ammonia produced surface area changes. NaOH treatment, the amorphous silica surface partially dissolved, and an aluminosilicate composite formed after aluminum salt application. The resulting composition occurred on the surface of the diatomites and the surface of the broader macros and mesopores. With these formations, significant increases in the specific surface areas of the diatomite samples from an initial 37.5 m^2 /g to 81.8 m^2 /g were also observed (Datsko et al., 2011). In a study on Manganese (Mn), the scientists Limei Chen, Zhixian, and others (Chen et al., 2021) used modified diatomites to investigate adsorption kinetics and isotherm mechanism. They altered the natural diatomite by applying acetic acid and sodium hydroxide to adsorbed Manganese.

The scientists also studied effective structural changes in groups of diatomite treated with acetic acid and alkali (Chen et al., 2021) using precise methods; they identified resulting formations and morphological architecture, including Fourier Transform Infrared, Scanning Electron Microscopy, and Brunauer-Emmett-Teller.

1.2. Origins of Saudi Arabian diatomite in the Nafud

Much of the Nafud desert, where pure diatomite deposits exist, has not been fully explored nor adequately mapped. Soft diatomites have been discovered and are perhaps more fragile than the known lakes of marl (sand, silt, or clay) and gypsum. They are likely to be buried, protected, and conserved under moving sands. Volcanic activity probably influenced the origins of diatomites in Bi'r Al Heezaa. (Whitney and Gettings, 1982). Superabundant amounts of Silica from the basalt plateaus to the west and south of the Nafud sand arm could have hastened the production of diatoms in specific deposit areas. It is also possible that diatomite deposits formed during a more ancient pluvial occurrence before the formation of the carbonate lake beds. The fact that there is 2 m or more of pure and nearly pure diatomite suggests its origins are in a giant freshwater lake of several kilometers in area. However, the lake shoreline is not visible. A shallow lake bed curve at the northeast also indicates basin diatomite deposits along its downward trajectory. Additionally, the high purity of the diatomite implies that the dunes in the region were not much contaminated and that the vegetation preserved it. It also suggests the absence of constant winds when lake sedimentation occurs (Whitney and Gettings, 1982; Whitney et al., 1983; Edgell, 2006).

1.3. Characteristics of diatomite in Saudi Arabia

In Saudi Arabia, there are diatomite deposits in the Tabuk in the North West region of the kingdom, specifically in the central Nafud sand sea desert, the southwest area of the Nafud arm at Bi'r Al Heezaa (Bi'r Al Haydhan). The known deposit is an exposed rocky outcrop of a transverse dune on a windward side). Other known deposits contain carbon or gypsum rocky outcrops. Other less exposed outcrops require further investigation. Much of this vast sea sand terrain consists of countless traverse dune ridges produced by a persistent westerly wind over a long period. Massive barchanoid dunes intersperse these traverse ridges. Many barchanoid slip faces may reach up to 100 m in height and have a 160 m difference between their lowest and highest points.

The terrain is composed of ever-moving, encroaching, and enveloping waves of sand. Due to the dense packing of wind-cast sands, the interdunal basins (dried freshwater lakes) are rarely visible. Consequently, this may be why so few diatomite deposits are so far discernible. Strong winds, shifting sand, and changing dune patterns have likely resulted in burying and eroding many diatomite deposits (Whitney and Gettings, 1982).

1.4. Volcanoes and silica

Volcanic activity may have influenced the original formation of diatomites in Bi'r Al Heezaa. Abundant amounts of Silica from the basalt plateaus to the west and south of the Nafud sand arm could have hastened the production of diatoms in specific deposit areas. It is also possible that diatomite was deposited during a more ancient pluvial occurrence prior to the formation of the carbonate lake beds. The fact

that there are 2 m and or more of pure and nearly pure diatomite suggests that the deposit origins are in a giant freshwater lake of several kilometers in area. (Whitney and Gettings, 1982; Cummins and Mulryan, 1949). Today, the shoreline is not clearly visible. However, a shallow lake bed curve at the northeast suggests that basin diatomite deposits may be located along its downward trajectory.

Additionally, the high purity of the diatomite implies that the dunes in the region did not get so contaminated and may have been preserved by vegetation.

It also suggests an absence of constant solid winds during the periods when lake sedimentation occurred. In general, diatomites are composed of Silica and water, about 2–8 %.

The amount of silica deposits contains determines its purity. The following amounts of Silica, alumina, iron and other elements comprise known samples of diatomites sourced worldwide (Whitney and Gettings, 1982; Cummins and Mulryan, 1949). For scientists to accomplish audit study objectives, a comprehensive data collecting and validation procedure is necessary. Omitting accuracy requirements will significantly limit the capacity to draw conclusions and likely generate less reliable results. Potentially, this would lead to obfuscation in the usage of characterization materials equipment. As a result, the primary goal of this study is to effectuate and optimise a complete data design for physical properties such as BET surface area, Langmuir surface area, *t*-plot micropore area, and quantity adsorbed based on a variety of heating times. Then, it will report a complete statistical optimization data set with independent variables and their responses.

Nowadays, response surface methodology (RSM) is in high demand in studying materials science, health, and the environmental sector (Manirul Haque, 2022a,b; Azmi et al., 2022; Sirhan Al-Batty et al., 2022). This RSM methodology reduces the number of experimental trials (Hossain et al., 2022) required, conserves lab instruments and devices (Zhou et al., 2021), and ultimately reduces analytical costs. A magnetic graphene oxide (Sheikhmohammadia et al., 2019) was studied using a central underwater composite design (RSM) methodology to optimize an appropriate functional relationship between the response and related input variables by RSM using R software. The best model to forecast and optimize GFM composite nanomaterials was determined to be the second-order model (Sheikhmohammadia et al., 2019).

In addition, the RSM assessed the rate of cyanide reduction in aqueous solutions by adsorption to the magnesium composite diatomite doped with alginate polymer beads (DMBA). The highest value of the correlation coefficient (0.92) was adopted as the appropriate model for the adsorption process, proving that RSM is an effective experimental technique for designing a statistical equation (Rasoulzadeh et al., 2021). The degradation of nonylphenol polyethoxylates (NPEs) was also studied using persulfate (PS) activated by naturally occurring semiconductor pyrite minerals (NP-SCM) in aqueous solutions. Effects of various factors, including solution pH, NP-SCM dose, NPE, and PS concentrations, were examined using the RSM and the Box-Behnken Design Technique (BBD). The impact of several factors, including the solution pH, NP-SCM dose, NPE, and PS concentrations, were examined using the Response Surface Method (RSM) and the Box-Behnken Design Technique (BBD) (Asgari et al., 2020). In addition, the optimization of data revealed by the response surface methodology using R software adsorption onto alginate beads impregnated with magnetic diatomite (ABMD) helped to investigate the decrement rate of triclosan (TCS) in aqueous solutions. Due to the 0.05 lack of fit and the larger R2 in the other models, the second-order model was selected as the most suitable one (Rasoulzadeh et al., 2021).

The objective of this study is to optimize the physical adsorption–desorption design of natural diatomite from Saudi Arabia. In this regard, seventeen trial runs were used to create the significant composite factor. Furthermore, Box-Behnken simulations were chosen to investigate and discover more about nearby and natural diatomites, permitting extended future investigation. To date, the research literature has yet to provide a modeling and optimization approach for the Saudi Arabian diatomite that includes its physical characteristics.

2. Experimental

2.1. Materials and chemical compositions

In Saudi Arabian, natural diatomite was collected from the North West of the kingdom. These diatomite sediments are located in the central Nafud sand sea desert, which is 300 km long and 200 km wide, specifically in the southwest area of the Nafud arm at Bi'r Al Heezaa (Bi'r Al Haydhan). The deposits are 300 km due north of the city of Madina Al Munawara and 70 km east of the ancient city of Tayma (Whitney et al., 1983). The known deposit is an exposed rocky outcrop of a transverse dune on a windward side—analysis of the chemical composition by X-ray fluorescence spectroscopy (XRF) (S8 TIGER de Bruker).

2.2. XRD

This research was performed with a Seifert-FPM 7 XRD diffractometer. The applied emission was Co K-alpha with a Fe filter. The X-ray tube parameters were 35 kV/25 mA with a 2θ scatter angle (4 for halloysite and 7 for diatom earth) for phase analysis up to 60–90.

2.3. Physical characterizations and conditions

The surface area study was performed with natural Bi'r Al Haydan diatomites. Samples were pulverized and passed through a metal particle sieve (250 μm). After being washed in distilled water, 0.2 g of the non-chemically treated powdered material was dried in an oven for four hours at 40 °C after being washed in distilled water. The Natural Diatomite sample was subjected to the isotherm characteristics of the sample by using; Brunauer-Emmet-Teller (BET) and the Barrett-Joyner-Halenda (BJH), mainly to establish surface areas and total pore distributions using the Micromeritics Gemini 2375 and Gemini V. instrument. Then, in a programmable furnace, an amount of diatomite was heated at temperature levels starting at room temperature and reaching up to 140 °C. The heating rate was set to rise at 10 °C per min. Intervals but without any acid or purification treatment. Samples were heated and investigated after 6, 12, 18, and 24 h. Subsequently, a sample of each operating period was analyzed to determine the pore surface morphology, size, and volume using the Gemini 2375 and Gemini V Micromeritics instrument.

2.4. Central composite experimental design

The current investigation involved a factorial design for response surface methodology – central composite design optimization (Manirul Haque and Box-Behnken, 2022). The statistical experiments were designed using the Design-Expert software (free trial 10.0.7.0 version). They randomly conducted 17 experiments to optimize Isotherm, BET surface area, Langmuir surface area, and *t*-plot Micropore area conditions.

Response surface graphs were employed to evaluate the factor correlation between the independent variables. The independent variables are for isotherm: a. heating time (hour), B. elapsed time (minute); BET surface area: a. heating time (hour), B. relative pressure; Langmuir surface area: a. heating time (hour), B. pressure (mmHg); *t*-plot Micropore area: a. heating time (hour), B. relative pressure against the quantity adsorbed (cm^3/g).

The analysis of variance (ANOVA), contour plots, and response surfaces assisted in evaluating the response model's statistical and correlation interaction between dependent and independent variables. Remarkably, the design provided to assess the results concerning the concurrent factor discrepancies in the studied trial sections to enhance the experimental settings. The correlation coefficient (R^2) conveyed the fitted model's quality. In contrast, the F-test assessed its geometric importance at the 5 % confidence level and confirmed the regression coefficients were expanding. The *t*-test comprised only significant coefficients with a p-value < 0.05. The optimum processing constraints were acquired via the desirability function based on the response by applying graphical and numerical analysis.

3. Results and discussion

3.1. Chemical composition

The percentage weight of Silica (86.3 %), Alumina (1.1 %), and Iron Fe_2O_3 (2.21 %), with ignition losses (7.9 %). The chemical composition of the samples also contained other trace elements, including calcium oxide CaO, phosphorus pentoxide P_2O_5, Magnesium Oxide MgO, Sodium Oxide Na_2O, and Titanium Oxide TiO_2. Moreover, the contamination level of the samples was low. The Silica's high content and its low quantities of alumina, iron, and lime serve as proof. Table 1 compares the results obtained in this investigation and others in the previous literature. (Whitney et al., 1983) and pointed to a close comparison.

3.2. XRD

All diatomite samples (white color) collected were found to have broad peaks in the Cristobalite Peak area. The principal quartz spike was seen in diatomite samples and small samples. This quartz spike indicates the presence of quartz silt grains, as these small amounts of clay are likely to be present in the lake bed.

3.3. Results of experimental physical characterization of the central composite and optimization of its design.

By altering the essential parameters and their impact, RSM-CCD normalizes the process and produces a second-degree polynomial model. The quadratic model estimated the higher F and regression coefficient value, lower standard deviation, and higher p-value. The ANOVA confirmed the model's increased significance, which was accomplished with p values < 0.05. With only 17 experimental runs, the study's likely isotherm, BET surface area, Langmuir surface area, and *t*-plot Micropore area can be determined using the quantity adsorbed (cm^3/g). (Tables 2–5). A multi-regression analysis was generated based on their experimental data between independent factors against its dependent variable as a response to predicted values and in accordance with the empirical findings. The following equation can be used to calculate the predicted adsorbed quantity using the second-order polynomial expression:

With coded formula

Isotherm:

Quantity adsorbed = $44.44 + 4.69\,a + 3.6B + 1.45\,aB - 6.60\,a^2 - 17.20\,B^2$.

BET surface area:

Quantity adsorbed = $15.62 + 0.6525\,a + 1.88B - 0.0723\,aB - 0.5063\,a^2 - 0.1850\,B^2$.

Langmuir surface area:

Quantity adsorbed = $16.89 + 0.5151\,a + 1.82B + 0.2651\,aB - 0.6551\,a^2 - 0.9309\,B^2$.

t-plot Micropore area:

Quantity adsorbed = $16.89 + 0.5151\,a + 1.82B + 0.2651\,aB - 0.6551\,a^2 - 0.9309\,B^2$.

With uncoded formula

Isotherm:

Quantity adsorbed = [- 44.74 + (1.67 × Heating time) + (36.63 × Elapsed time) + {0.08×(Heating time × Elapsed Time)} – (0.08 × Heating time^2) – (4.36 × Elapsed time^2)].

BET surface area:

Table 1 Chemical composition comparison for the Bi Al Heezaa diatomite from different sources.

	Current results	**Comparison with the literature** (Whitney et al., 1983)					
Consistent (%)	Bi'r Al Heezaa	Bi'r Heezaa	Lombpoc, Ca	Maryland	Russian Urlas	Kenya	Algeria
Silica (SiO_2)	86.3	85.0	98.70	79.55	79.92	84.50	58.40
Alumina (Al_2O_3)	1.1	1.40	3.72	8.18	6.58	3.06	1.66
Lime (CaO)	0.39	0.43	0.30	0.25	3.00	1.80	13.80
Magnesia (MgO)	0.21	0.21	0.55	1.30	0.81	0.39	4.57
Sodium Oxide (Na_2O)	0.21	0.18	0.31	1.31	0.50	1.19	0.96
Potassium Oxide (K_2O)	0.2	0.20	0.41	2.62	0.39	0.91	0.50
Iron Oxide (Fe_2O_3)	2.21	2.34	1.09	0.70	3.56	1.86	1.55
Titanium, Oxide (TiO_2)	0.09	0.10	0.10	0.70	0.48	0.17	0.10
Phosphate (P_2O_5)	0.08	0.07	0.20	–	–	0.04	0.20
Ignition Loss (LOI)	7.9	8.27	3.70	5.80	5.20	6.08	17.48
Total	**98.69**	**98.2**	**99.98**	**99.71**	**99.37**	**100**	**99.22**

Table 2 Central composite design with isotherm included independent variables and their response.

Runs	a. Heating time (Hour)	B. Elapsed time (minute)	Quantity adsorbed (cm^3/g)	
			Experimental	Predicted
1	6	1.27	3.38	3.32
2	6	6.89	12.28	12.14
3	0	2.09	13.77	13.79
4	0	6.06	18.01	18.10
5	18	2.09	20.15	20.28
6	18	6.06	30.21	30.37
7	12	4.08	45.11	45.27
8	12	4.08	45.11	45.27
9	12	4.08	45.11	45.27
10	12	4.08	45.11	45.27
11	12	4.08	45.11	45.27
12	12	4.08	45.11	45.27
13	24	4.08	33.78	33.93
14	24	4.08	33.78	33.93
15	12	4.08	45.55	45.27
16	12	4.08	45.55	45.27
17	12	4.08	45.55	45.27

Table 3 Central composite design with BET surface area included independent variables and their response.

Runs	a. Heating time (Hour)	B. Relative pressure	Quantity adsorbed (cm^3/g)	
			Experimental	Predicted
1	6	0.03	12.28	12.26
2	6	0.23	17.67	17.69
3	0	0.06	12.32	12.31
4	0	0.20	16.23	16.23
5	18	0.06	13.77	13.79
6	18	0.20	17.39	17.39
7	12	0.13	15.78	15.79
8	12	0.13	15.78	15.79
9	12	0.13	15.78	15.79
10	12	0.13	15.78	15.79
11	12	0.13	15.78	15.79
12	12	0.13	15.78	15.79
13	24	0.13	15.3	15.28
14	24	0.13	15.3	15.28
15	12	0.13	15.78	15.79
16	12	0.13	15.78	15.79
17	12	0.13	15.78	15.79

Table 4 Central composite design with Langmuir surface area included independent variables and their response.

Runs	a. Heating time (Hour)	B. Pressure (mmHg)	Quantity adsorbed (cm^3/g)	
			Experimental	Predicted
1	6	9.79	12.33	12.35
2	6	250.21	17.24	17.22
3	0	45	13.23	13.26
4	0	215	16.35	16.35
5	18	45	13.73	13.73
6	18	215	17.91	17.94
7	12	130	16.99	16.99
8	12	130	16.99	16.99
9	12	130	16.99	16.99
10	12	130	16.99	16.99
11	12	130	16.99	16.99
12	12	130	16.99	16.99
13	24	130	15.93	15.94
14	24	130	15.93	15.94
15	12	130	16.99	16.99
16	12	130	16.99	16.99
17	12	130	16.99	16.99

Table 5 Central composite design with *t*-plot micropore area included independent variables and their response.

Runs	a. Heating time (Hour)	B. Relative pressure	Quantity adsorbed (cm^3/g)	
			Experimental	Predicted
1	6	0.11	15.45	15.44
2	6	0.74	26.59	26.58
3	0	0.20	15.28	15.27
4	0	0.65	22.92	22.92
5	18	0.20	17.35	17.36
6	18	0.65	25.7	25.71
7	12	0.425	21.26	21.26
8	12	0.425	21.26	21.26
9	12	0.425	21.26	21.26
10	12	0.425	21.26	21.26
11	12	0.425	21.26	21.26
12	12	0.425	21.26	21.26
13	24	0.425	20.4	20.42
14	24	0.425	20.4	20.42
15	12	0.425	21.26	21.26
16	12	0.425	21.26	21.26
17	12	0.425	21.26	21.26

Quantity adsorbed = [10.19 + (0.19 × Heating time) + (37.74 × Relative pressure) – {0.12×(Heating time × Relative pressure)} – (0.01 × Heating time^2) – (37.76 × Relative pressure^2)].

Langmuir surface area:

Quantity adsorbed = [11.16 + (0.16 × Heating time) + (0.05 × Pressure) + {0.0003×(Heating time × Pressure)} – (0.01 × Heating time^2) – (0.0001 × Pressure^2)].

t-plot Micropore area:

Quantity adsorbed = [12.61 + (0.3 × Heating time) + (12.21 × Relative pressure) + {0.09×(Heating time × Relative pressure)} – (0.01 × Heating time^2) + (5.61 × Relative pressure^2)].

But pressure variations are what most significantly contribute to the Langmuir surface area. However, relative pressure and its combined effects with heating may affect how the sample adsorbs in the *t*-plot micropore area. The quadratic model's response surface fit can be evaluated for precision using the analysis of variance (ANOVA). The chosen model must have higher F values and a p-value of at least 0.0001, demonstrating the model's importance (Tables 6–9). It was discovered that the elapsed time had a more significant impact on the isotherm to adsorbed quantity than the heating duration. It might also be affected by the square value of the time that has passed and the result of adding heating. The square of the

Table 6 The quadratic model concerning isotherm with F and p values.

Source	Term df	Error df	F-value	p-value	
Whole-plot	1	4.95	16397.01	< 0.0001	Significant
B^2	1	4.95	16397.01	< 0.0001	
Subplot	4	6.74	42286.87	< 0.0001	Significant
a-Heating time	1	4.95	924.87	< 0.0001	
B-Elapsed time	1	5.98	97181.70	< 0.0001	
aB	1	5.98	8702.41	< 0.0001	
a^2	1	5.24	7105.27	< 0.0001	

Table 7 The quadratic model concerning BET surface area with F and p values.

Source	Term df	Error df	F-value	p-value	
Whole-plot	3	11.00	8.026E + 06	< 0.0001	Significant
a-Heating time	1	11.00	1.071E + 07	< 0.0001	
a^2	1	11.00	1.178E + 07	< 0.0001	
B^2	1	11.00	1.152E + 06	< 0.0001	
Subplot	2	11.00	8.111E + 07	< 0.0001	Significant
B-Relative pressure	1	11.00	1.520E + 08	< 0.0001	
aB	1	11.00	1.248E + 05	< 0.0001	

Table 8 The quadratic model concerning Langmuir surface area with F and p values.

Source	Term df	Error df	F-value	p-value	
Whole-plot	3	11.00	4.510E + 07	< 0.0001	Significant
a-Heating time	1	11.00	1.140E + 07	< 0.0001	
a^2	1	11.00	3.368E + 07	< 0.0001	
B^2	1	11.00	4.982E + 07	< 0.0001	
Subplot	2	11.00	1.237E + 08	< 0.0001	Significant
B- Pressure	1	11.00	2.440E + 08	< 0.0001	
aB	1	11.00	2.862E + 06	< 0.0001	

Table 9 The quadratic model concerning *t*-plot micropore area with F and p values.

Source	Term df	Error df	F-value	p-value	
Whole-plot	3	2.00	3.955E + 05	< 0.0001	Significant
a-Heating time	1	2.00	1.688E + 06	< 0.0001	
a^2	1	2.00	1.521E + 06	< 0.0001	
B^2	1	2.00	1.009E + 05	< 0.0001	
Subplot	2	9.00	4.736E + 09	< 0.0001	Significant
B-Relative pressure	1	9.00	9.123E + 09	< 0.0001	
aB	1	9.00	9.988E + 06	< 0.0001	

elapsed time and the combined effect of elapsed time and heating may also have an impact.

In contrast, the relative pressure and square values were more critical during the quantity adsorbed in the case of BET surface area. However, the most significant contribution to the Langmuir surface area is made by pressure factors. Based on the *t*-plot micropore area, relative pressure and its combined effect with heating could affect the sample's adsorption. In addition, the response model might represent 100 % variability with a determination coefficient of 1, corresponding to the quadratic model. Isotherm, BET surface, Langmuir, and *t*-plot micropore design's predicted values were close to the

mean values, demonstrating the model's excellent predictability. The predicted R2 (1) is satisfied with the adjusted R2 (1) and the lack of fit values of 0.0006, 7.55×10^{-8}, 4.42×10^{-8} and 6.28×10^{-9} respectively,

A case study of pyrrole adsorption on natural diatomite from Saudi Arabia was described in the literature (Alsawalha et al., 2019), employing temperature-programmed desorption of pyrrole and regression analysis maths modeling. As a result, it was determined that the activation energy was crucial during the adsorption step (Alsawalha et al., 2019). Evaluation of the statistical and correlation interaction between dependent and independent variables in the response model was aided by the study of ANOVA (Alsawalha et al., 2019), contour plots, and response surfaces. The qualitative and quantitative aspects have also been covered in the literature (Alsawalha et al., 2019; Anderson-Cook et al., 2009; You et al., 2021; Raymaekers and Rousseeuw, 2021). Remarkably, the design offers a way to evaluate the findings about concurrent factor disparities in the investigated trial sections to improve the experimental conditions. The quality of the fitted model was expressed by the correlation coefficient (R2). In contrast, the F-test determined its geometric importance at the 5 % confidence level and validated the expanding regression coefficients. Only significant coefficients with a p-value of < 0.05 were included in the *t*-test.

The actual predicted plot is a scatter plot, allowing for a visual assessment of potential fit issues. A fair estimate must yield anticipated values that, on average, correspond with the observed values. A complete model analysis contrasts the entire model with all the factors added to the intercept for the alternative hypothesis with the model with only intercepts for the null hypothesis. As a result, these models can be used to evaluate the responses. The expected and actual results are compared (Fig. 1a, 1d, 1 g, and 1j). The observed values resemble the expected value very well. The expected response values for each run are typically dispersed over a straight line.

A Box-Cox is a transformation of non-typical dependent factors into a standard shape (Larouci et al., 2015). It is an essential hypothesis for the statistical procedures in which abnormal data applying a Box-Cox means that it can run a more significant number of experiments. The model was investigated with each crucial transformation, confirming that no conversion is necessary (Fig. 1b, 1e, 1 h, and 1 k). The pertur-

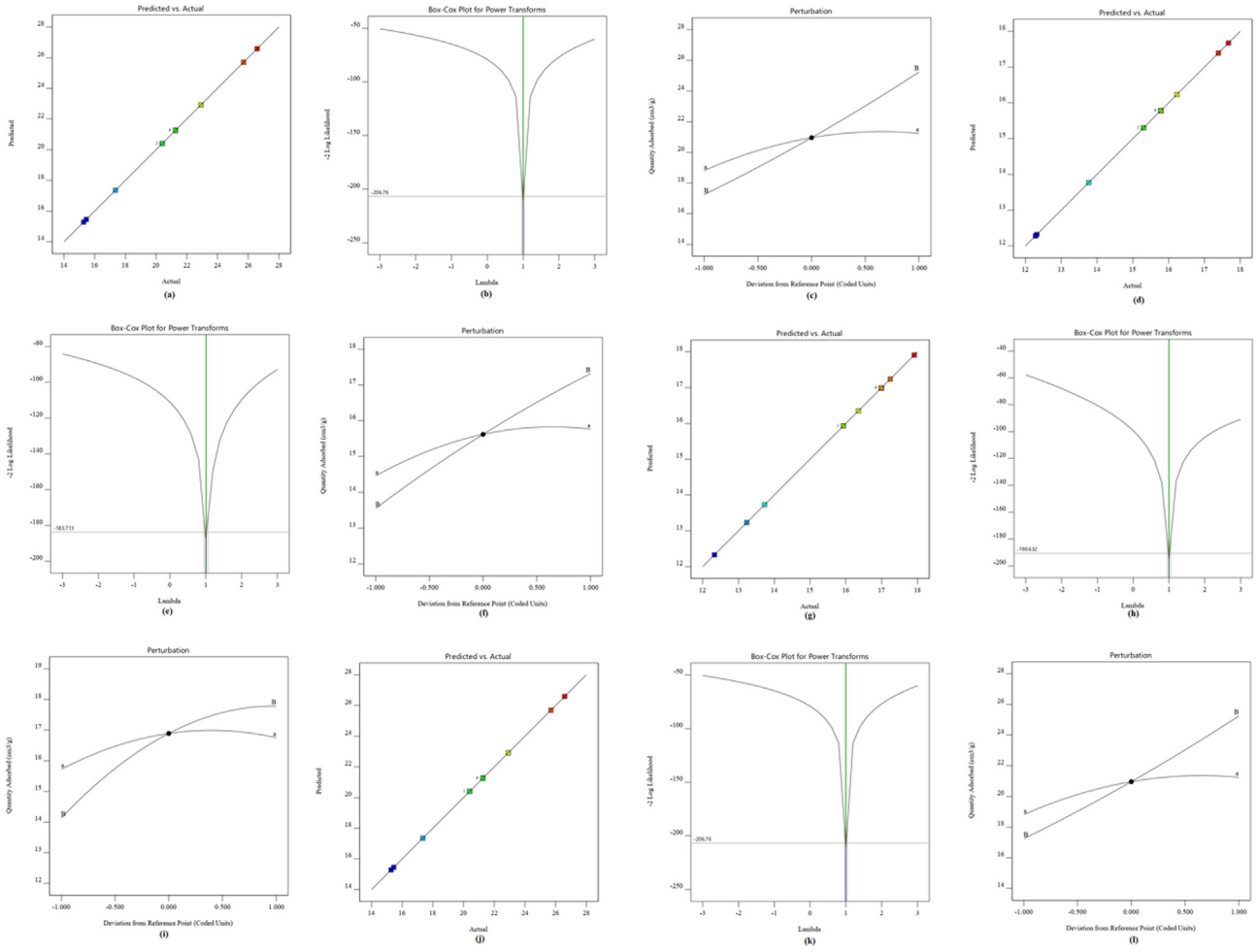

Fig. 1 Central composite design for *isotherm* with tested variables (a) Predicted vs Actual (b) Box-Cox plot for power transforms (c) Perturbation; for *BET surface area*: (d) Predicted vs Actual (e) Box-Cox plot for power transforms (f) Perturbation; for *Langmuir surface area*: (g) Predicted vs Actual (h) Box–Cox plot for power transforms (i) Perturbation; for *t-plot micropore area*: (j) Predicted vs Actual (k) Box–Cox plot for power transforms (l) Perturbation.

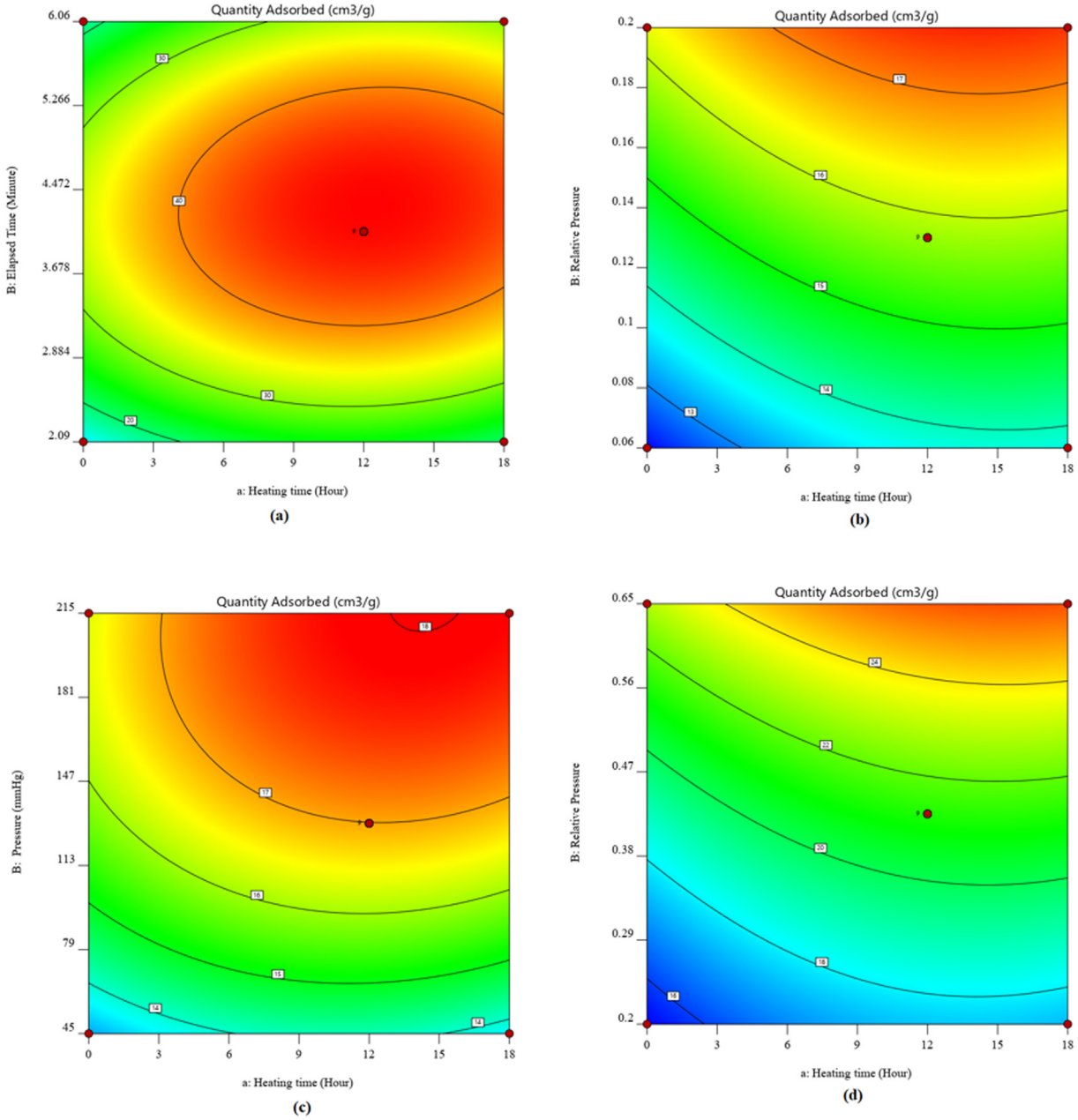

Fig. 2 2D contour plot due to the effect of (a) heating time and elapsed time for isotherm, (b) heating time and relative pressure for BET surface area, (c) heating time and pressure for Langmuir surface area, (d) heating time and relative pressure for t–plot micropore area.

bation explains the significance of independent factors and their effect on the responses. The elapsed time was adequate with the heating time (Fig. 1c).

In contrast, in other cases (Fig. 1f, 1i, 1 l), pressure and relative pressure were more influential in the responses. The contour graph exhibits a relationship between two independent factors and a dependent. The plot indicates the response values for combinations of independent variables. It is effective when identifying independent variable combinations that deliver favorable dependent values. The advantage of the 3D surface graphs is that they explain the corresponding response factors to two predictors available for different types of investigations (Jumah et al., 2021; Yun et al., 2022; Liu et al., 2020; Piri et al., 2021). It is a valuable three-dimensional graph for considering desired response values with operating requirements. The heating time, elapsed time, pressure, and relative pressure against the dependent variable were clarified with 3D surface and contour plots. The earlier investigation on the natural diatomite has shown that significantly higher heating ranges between 600 °C and 1200 °C have led to a change in the structure of the materials (Ibrahim and Selim, 2012). The plots disclosed that the adsorbed quantities were well-depended on heating time, elapsed time, pressure, relative pressure for isotherm, BET surface area, Langmuir surface area, and *t*-plot micropore area, and this is in agreement with the literature (Bello et al., 2014). As a result, the responses to the variables in Figs. 2

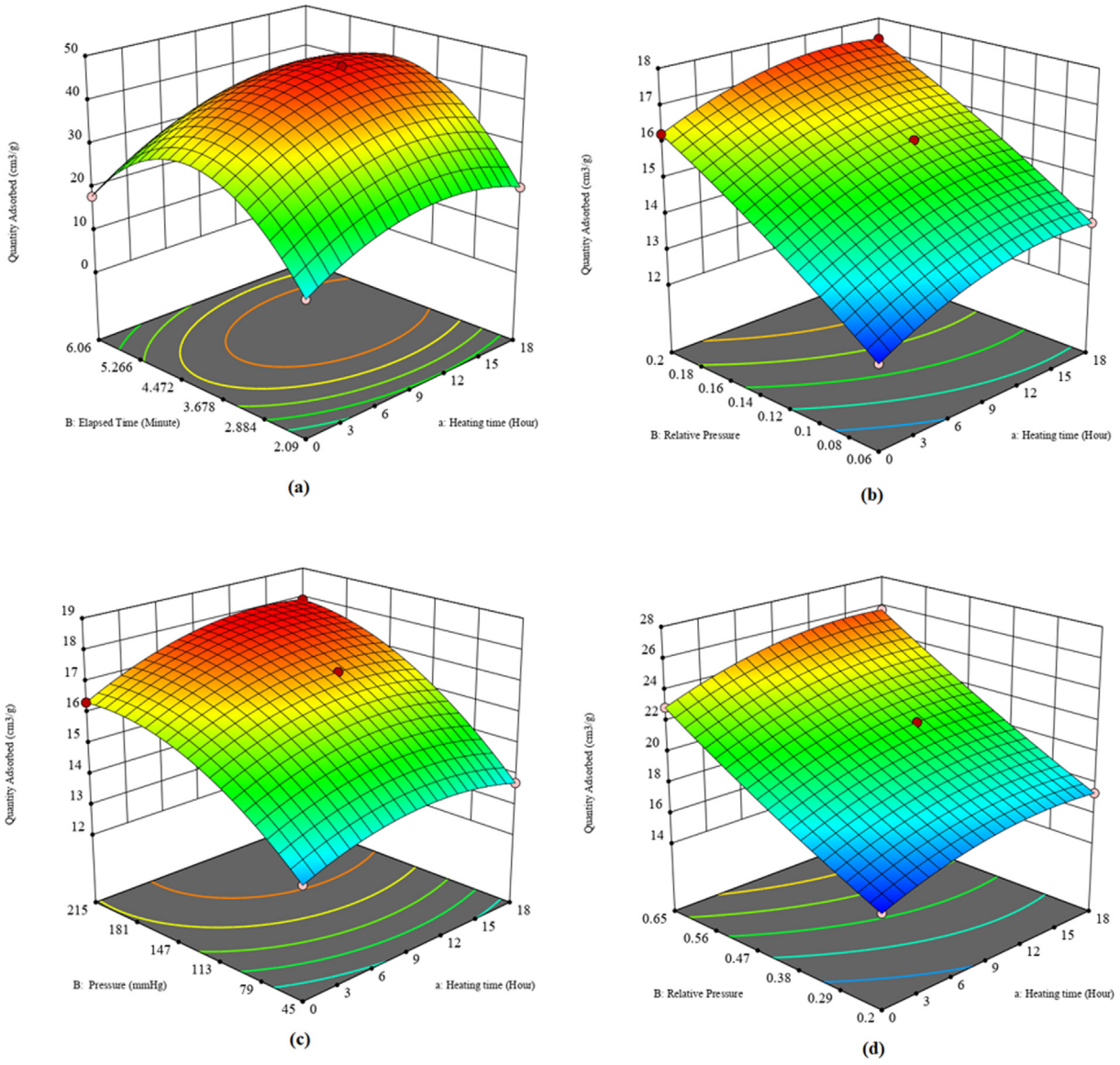

Fig. 3 3D surface plot due to the effect of (a) heating time and elapsed time for isotherm, (b) heating time and relative pressure for BET surface area, (c) heating time and pressure for Langmuir surface area, (d) heating time and relative pressure for t–plot micropore area.

and 3 were inconsistent. The amount of adsorbed material rose as heating time and elapsed time increased; however, after 12.716 h of heating, it began to degrade according to isotherm. The BET surface also produced similar results. Here, relative pressure increased the material adsorbed with a heating time of 3.254 hrs. The heating time, pressure, and relative pressure were also used to create Langmuir and *t*-plot. The adsorbed quantity initially increased with the addition of independent parameters but eventually started to decline and was optimized using the RSM-CCD, as shown below. The amount adsorbed initially increased with the addition of independent parameters but eventually started to fall and was optimized using the RSM-CCD, as shown below.

The following are the optimum experimental conditions for desirability-one:*Isotherm:*
Heating time – 12.716 (hour).
Elapsed time – 4.825 (minute).
Adsorbed quantity – 44.379 (cm^3/g).
BET surface area:
Heating time – 3.254 (hour).
Relative pressure – 0.078.
Adsorbed quantity – 13.458 (cm^3/g).
Langmuir surface area:
Heating time – 5.243 (hour).
Pressure – 122.879 (mmHg).
Adsorbed quantity – 16.412 (cm^3/g).
t-plot Micropore area:
Heating time – 3.342 (hour).
Relative pressure – 0.416.
Adsorbed quantity – 19.682 (cm^3/g).

4. Conclusions

The findings offer a thorough examination and a coherent account of the simultaneous influence of independent variables, such as temperature and relative pressure, on the morphology of natural diatomite surfaces. The F test verified that the regression coefficients had increased and assessed its geometric significance at the 5 % level. The *t*-test only included significant coefficients with a $p < 0.05$, and pressure and relative pressure significantly impacted the results. On the other hand, the contour graph showed a relationship between two independent components, with an R2 coefficient of dependency and correlation representing the quality and how well the updated model worked. Finally, the current data research can aid scientists in scaling up the production and usage of local materials for a variety of industries, including pharmaceutical manufacture, environmental and water treatment, industrial catalysts, and cement-based additives.

Declaration of Competing Interest

The authors declare that they have no known competing financial interests or personal relationships that could have appeared to influence the work reported in this paper.

Acknowledgments

Thanks and appreciation belong to King Abdulaziz City for Science and Technology for its facility and analysis of material properties. The author would like to thank Dr. SK Manirul for his outstanding support and the fruitful discussion on statistical data analysis and overall work review. I very much appreciate the support of Professor Abdulaziz from King Abdulaziz City for Science and Technology in analyzing the samples. The author also gratefully acknowledges Mr. Mohammed Francis for all the editing and fruitful discussion. Appreciations are also extended to Jubail Industrial College for cooperation and encouragement.

References

Acharya, L., Swain, G., Mishra, B.P., Acharya, R., Parida, K., 2022. Development of MgIn2S4 Microflower-Embedded Exfoliated B-Doped g-C3N4 Nanosheets: p–n Heterojunction Photocatalysts toward Photocatalytic Water Reduction and H_2O_2 Production under Visible-Light Irradiation. ACS Applied Energy Materials 5 (3), 2838–2852. https://doi.org/10.1021/acsaem.1c03525.

Akin, S., Schembre, J.M., Bhat, S.K., Kovscek, A.R., 2000. Spontaneous imbibition characteristics of diatomite. J. Petrol. Sci. Eng. 25, 149–165.

Murad Alsawalha, Chintaginjala Venkateswara Rao, Abeer Mohammed Al-Subaie, SK Manirul Haque, Vishnu Priya Veeraraghavan, Krishna Mohan Surapaneni, 2019. Materials Reserch and Express, Vol.6, p.105531, https://iopscience.iop.org/article/10.1088/2053-1591/ab2f9b.

Anderson-Cook, Christine M., Borror, Connie M., Montgomery, Douglas C., 2009. Response surface design evaluation and comparison. Journal of Statistical Planning and Inference 139 (2), 629–641. https://doi.org/10.1016/j.jspi.2008.04.004. ISSN 0378-3758.

Araújo do Nascimento, Clístenes Williams, Vieira da Silva, Fernando Bruno, Araújo, Paula Renata Muniz, Araújo, Josângela do Carmo Trezena de, Lins, Simone Aparecida da Silva, 2021. Efficiency and recovery index of silicon of a diatomaceous Earth-based fertilizer in two soil types grown with sugarcane and maize. J. Plant Nutr. 44 (16), 2347–2358. https://doi.org/10.1080/01904167.2021.1918157.

Asgari, E., Mohammadi, F., Nourmoradi, H., Sheikhmohammadi, A., Rostamifasih, Z., Hashemzadeh, B., Arfaeinia, H., 2020. Heterogeneous catalytic degradation of nonylphenol using persulphate activated by natural pyrite: response surface methodology modeling and optimisation. Int. J. Environ. Anal. Chem. https://doi.org/10.1080/03067319.2020.1807528.

Azmi, S.N.H., Al-Masrouri, Z.N., Al-Lamki, I.R., Al-Jabri, A.K., Rahman, N., Nasir, M., Abdelrahman, K., Fnais, M.S., Alam, M., 2022. **2022**, development and validation of spectrophotometric method for determination of imipramine hydrochloride in tablets (solid materials). J. King Saud Univ. Sci. 34,. https://doi.org/10.1016/j.jksus.2022.101823 101823.

Battarbee, R.W., Jones, V.J., Flower, R.J., Cameron, N.G., Bennion, H., Carvalho, L., 2002. Juggins, S. Diatoms. In: Smol, J.P., Birks, H.J.B., Last, W.M., Bradley, R.S., Alverson, K. (Eds.), Tracking Environmental Change Using Lake Sediments Volume 3: Terrestrial, Algal, and Siliceous Indicators. Springer, Dordrecht, pp. 155–202.

Bello, O.S., Adegoke, K.A., Oyewole, R.O., 2014. Insights into the Adsorption of Heavy Metals from Wastewater using Diatomaceous Earth. Sep. Sci. Technol. 49 (12), 1787–1806. https://doi.org/10.1080/01496395.2014.910223.

Chen, L., Li, Z., Li, W., Chen, Z., Chen, G., Yang, W., Zhang, X., Liu, X., 2021. Investigation of Adsorption Kinetics and the Isotherm Mechanism of Manganese by Modified Diatomite. ACS Omega 6 (25), 16402–16409. https://doi.org/10.1021/acsomega.1c01204.

Cummins, A.B., Mulryan, H., 1949. Chapter 13, Diatomite. In: Industrial Minerals and Rocks. 2nd ed.:. New York, American Institute of Mining and Metallurgical Engineers, pp. 294–312.

Datsko, T.Y., Zelentsov, V.I., Dvornikova, E.E., 2011. Physicochemical and adsorption-structural properties of diatomite modified with aluminum compounds. Surf. Engin. Appl. Electrochem. 47, 530–539. https://doi.org/10.3103/S1068375511060081.

Edgell, H. Stewart, 2006, Arabian sand seas. In: Arabian Deserts. Springer, Dordrecht., 125-166, Springer Netherlands, Dordrecht, , https://doi.org/10.1007/1-4020-3970-0_7.

Elias, M.L., Cultrone, G., 2019. On the Use of Sodium Chloride and Calcined Diatomite Sludge as Additives to Improve the Engineering Properties of Bricks Made with a Clay Earth from Jun (Granada, Spain)''. Minerals 9 (1), 64. https://doi.org/10.3390/min9010064.

Flower, R.J. 2013. diatom methods, Diatomites: Their Formation, Distribution, and Uses. In: Scott A. Elias, Cary J. Mock, (Eds.), Encyclopedia of Quaternary Science, Second Edition, Elsevier, Pp. 501-506, ISBN 9780444536426, https://doi.org/10.1016/B978-0-444-53643-3.00220-X.

Ghobara, M. M., Ghobara, M. M., Ghobara, M. M. and Mohamed, A. 2019. Diatomite in Use: Nature, Modifications, Commercial Applications, and Prospective Trends, Diatoms: Fundamentals and Applications, Jun 28, 471– 509.

Goren, R., Baykara, T., Marsoglu, M., 2002. A study on the purification of diatomite in hydrochloric acid. Scand. J. Metall. 31, 115–119. https://doi.org/10.1034/j.1600-0692.2002.310205.x.

Hanif, C.M.S., Mansha, M.Z., Aatif, H.M., et al, 2022. Aptness of entomogenus fungi with diatomaceous earth against various stored grain insect pests. Egypt J Biol Pest Control 32, 14. https://doi.org/10.1186/s41938-022-00514-w.

Harwood, D.M., 1999. Diatomite. In: Stoermer, E.F., Smol, J.P. (Eds.), the Diatoms: Applications for the Environmental and Earth Sciences. Cambridge University Press, Cambridge, pp. 436–446.

Hossain, S.M.Z., Sultana, N., Irfan, M.F., Manirul Haque, S.K., Nasr, N., Razzak, S.A., 2022. Artificial intelligence-based super learner approach for prediction and optimization of biodiesel synthesis -a case of waste utilization. Int. J. Energy Res. 46, 20519–20534. https://doi.org/10.1002/er.7764.

Huang, W., Lv, W., Chu, H., Lv, W., Zhou, W., Dong, B., 2021. Diatomite Dynamic Membrane Fouling Behaviour during Dewa-

tering of Chlorella pyrenoidosa in Aquaculture Wastewater. Membranes (Basel). 11 (12), 945. https://doi.org/10.3390/membranes11120945. PMID: 34940445; PMCID: PMC8706875.

Ibrahim, S.S., Selim, A.Q., 2012. Physicochem. Probl. Miner. Process. 48 (2), 413–424.

Janićijević, J., Krajišnik, D., Čalija, B., Vasiljević, B.N., Dobričić, V., Daković, A., Antonijević, M.D., Milić, J. 2015. Modified local diatomite as potential functional drug carrier–A model study for diclofenac sodium. Int J Pharm. Dec 30;4 96(2), 466-74. doi: 10.1016/j.ijpharm.2015.10.047. Epub 2015 Oct 21. PMID: 26498370.

Bin Jumah, May N., Ibrahim, Sherouk M., AL-Huqail, Arwa A, Bin-Murdhi, Nouf Saleh, Allam, Ahmed A., Abu-Taweel, Gasem M., Altoom, Naif, Al-Anazi, Khalid M., Abukhadra, Mostafa R., 2021. Enhancing the Catalytic Performance of NiO during the Transesterification of Waste Cooking Oil Using a Diatomite Carrier and an Integrated NiO Metal: Response Surface Studies, American Chemical Society, ACS Omega, V. 6, Issue DOI: 10.1021/acsomega.1c01301.

Fatma Kucuk, Sedef Sismanoglu, Yasin Kanbur, Umit Tayfun, 2020. effect of silane-modification of diatomite on its composites with thermoplastic polyurethaneMaterials Chemistry and Physics, 10.1016/j.matchemphys.2020.123683, (123683).

Larouci, M., Safa, M., Meddah, B., Aoues, A., Sonnet, P., 2015. Response surface modeling of acid activation of raw diatomite using sunflower oil bleaching by: Box-Behnken experimental design. J. Food Sci. Technol. 52 (3), 1677–1683. https://doi.org/10.1007/s13197-013-1113-9. PMID: 25745240; PMCID: PMC4348268.

Liu, Y., Zhang, J., Sheng, X., Li, N.a., Ping, Q., 2020. Adsorption and Release Kinetics, Equilibrium, and Thermodynamic Studies of Hymexazol onto Diatomite, ACS. Omega 5 (45), 29504–29512. https://doi.org/10.1021/acsomega.0c04449.

Liu, Y., Yang, W., Chen, Q., Cullen, D.A., Xie, Z., Lian, T., 2022. Pt Particle Size Affects Both the Charge Separation and Water Reduction Efficiencies of CdS–Pt Nanorod Photocatalysts for Light Driven H_2 Generation. J. Am. Chem. Soc. 144 (6), 2705–2715. https://doi.org/10.1021/jacs.1c11745.

Maher, S., Kumeria, T., Aw, M.S., Losic, D., 2018. Diatom Silica for Biomedical Applications: Recent Progress and Advances. Adv Healthc Mater. 7 (19), e1800552. https://doi.org/10.1002/adhm.201800552. Epub 2018 Aug 17. PMID: 30118185.

Managò, S., Tramontano, C., Delle Cave, D., Chianese, G., Zito, G., De Stefano, L., Terracciano, M., Lonardo, E., De Luca, A.C., Rea I. SERS, 2021. Quantification of Galunisertib Delivery in Colorectal Cancer Cells by Plasmonic-Assisted Diatomite Nanoparticles. Small. 2021 Aug;17(34):e2101711. doi: 10.1002/smll.202101711. Epub. PMID: 34302422.

Manirul Haque, S.K., 2022a. Validated Kinetic Spectrophotometric Methods to Optimize Robustness Study with Youden Factorial Combinations to Determine Repaglinide Using Response Surface Methodology via Box-Behnken Design. Arab J Sci Eng. https://doi.org/10.1007/s13369-022-06782-w.

Manirul Haque, S.K., 2022b. Optimized Box-Behnken experimental design based response surface methodology and Youden's robustness test to develop and validate methods to determine nateglinide using kinetic spectrophotometry. Spectrochim. Acta Part A Mol. Biomol. Spectrosc. 268,. https://doi.org/10.1016/j.saa.2021.120712 120712.

Manirul Haque, S.K., Box–Behnken, 2022. experimental design for optimizing the HPLC method to determine hydrochlorothiazide in pharmaceutical formulations and biological fluid, Journal of Molecular Liquids, Volume 352, 118708, ISSN 0167-7322, https://doi.org/10.1016/j.molliq.2022.118708.

Niu, F., Wenguang, T.u., Xinxin, L.u., Chi, H., Zhu, H., Xi Zhu, L.u., Wang, Y.X., Yao, Y., Zhou, Y., Zou, Z., 2022. Single Pd–Sx Sites In Situ Coordinated on CdS Surface as Efficient Hydrogen Autotransfer Shuttles for Highly Selective Visible-Light-Driven C-N Coupling. *ACS* Catalysis 12 (8), 4481–4490. https://doi.org/10.1021/acscatal.2c00433.

Piri, M., Sepehr, E., Samadi, A., Farhadi, K., Alizadeh, M., 2021. application of diatomite for sorption of Pb, Cu, Cd, and Zn from aqueous solutions: kinetic, thermodynamic studies and application of response surface methodology (RSM). Water Environ Res 93, 714–726. https://doi.org/10.1002/wer.1377.

Rachna, R.M., Shanker, U., 2020. Sunlight assisted degradation of toxic phenols by zinc oxide doped prussian blue nanocomposite. J. Environ. Chem. Eng. 8, 104040.

Rasoulzadeh, H., Sheikhmohammadi, A., Asgari, E., Hashemzadeh, B., 2021. The adsorption behavior of triclosan onto magnetic bio polymer beads impregnated with diatomite. Int. J. Environ. Anal. Chem. https://doi.org/10.1080/03067319.2021.1922684.

Rasoulzadeh, H., Sheikhmohammadi, A., Abtahi, M., Roshan, M.A. B., 2021. Predicting the capability of diatomite magnano composite boosted with polymer extracted from brown seaweeds for the adsorption of cyanide from water solutions using the response surface methodology: modeling and optimization. Int. J. Environ. Anal. Chem. https://doi.org/10.1080/03067319.2021.1931160.

Raymaekers, J., Rousseeuw, P.J., 2021. Transforming variables to central normality. Mach Learn. https://doi.org/10.1007/s10994-021-05960-5.

Ren, Z., He, Y., Zheng, R., Guo, Z., Gao, H., He, X., Feida, W.u., Ji, X., 2022. The preparation and characterization of calcined diatomite with high adsorption properties by CaO hydrothermal activation, Colloids and Surfaces A: Physicochemical and Engineering Aspects, 636. ISSN 128134, 0927–7757. https://doi.org/10.1016/j.colsurfa.2021.128134.

Sannikova, N. et al, 2021. Natural Reserves of Diatomite Areas a Component of Organomineral Fertilizers Based on Chicken Manure. IOP conference series. Earth and environmental science 937 (3), 32093.

Sheikhmohammadia, A., Mohsenib, S.M., Hashemzadeha, B., Asgaria, E., Sharafkhania, R., Sardarb, M., Sarkhoshc, M., Almasiane, M., 2019. Fabrication of magnetic graphene oxide nanocomposites functionalized with a novel chelating ligand for the removal of Cr(VI): Modeling, optimization, and adsorption studies. Desalin. Water Treat 160, 297–307.

Shen, Z., Fan, Q., Yu, Q., Wang, R., Wang, H., Kong, X., 2021. Facile detection of carbendazim in food using TLC-SERS on diatomite thin layer chromatography. Spectrochim Acta A Mol Biomol Spectrosc 247, 119037. https://doi.org/10.1016/j.saa.2020.119037. Epub 2020. PMID: 33086143.

Sirhan Al-Batty, S.K., Haque, M., Rahman, N., Azmi, S.N.H., 2022. Optimized Box-Behnken Design Combined Response Surface Methodology to Determine Calcium and Iron Contents Using Visible, Atomic Emission and Atomic Absorption Spectrophotometry in Vegetables and Wastewater Samples. J. AOAC Int. qsac106. https://doi.org/10.1093/jaoacint/qsac106.

Wang, M., Xiang, Y., Zhang, G., Song, J., Cai, D., Wu, Z., 2013. A facile approach to improve the quality of diatomite as sulfuric acid catalyst support. Appl. Catal. A Gen. 466, 185–189. https://doi.org/10.1016/j.apcata.2013.06.029.

Wang, M., Hongliang, X.u., Huang, C., Cui, Z., Li, M., Song, B.o., Shao, G., Wang, H., Hongxia, L.u., Zhang, R., 2021. Preparation of g-C_3N_4/diatomite composite with improved visible-light photocatalytic activity. Inorg. Chem. Commun. https://doi.org/10.1016/j.inoche.2021.108645, 129, (108645).

Wei, Y., Jie, G.u., Wang, X., Song, Z., Sun, W., Ting, H.u., Guo, H., Xie, J., Lei, L., Liang, X.u., Li, Y., 2022. Elucidating the beneficial effects of diatomite for reducing abundances of antibiotic resistance genes during swine manure composting, Science of The Total Environment, Volume 821. ISSN 0048–9697. https://doi.org/10.1016/j.scitotenv.2022.153199.

Whitney, J.W., Gettings, M.E., 1982. Open-File Report Vol. 1982 (82-1046), Preliminary geological investigation of the Bir Hayzan diatomite deposit, Kingdom of Saudi Arabia, with a section on

selected physical properties and implications for future geophysical exploration. US Geological Survey doi:10.3133/ofr821046 https://doi.org/10.3133/ofr82104.

Whitney, John W., Faulkender, D.J., Rubin, Meyer, 1983. Open-File Report Vol. 1983 (83-749), The environmental history and present condition of Saudi Arabia's northern sand seas. US Geological Survey doi:10.3133/ofr83749.

Gauvain Wiemer, Ricarda Dziadek, 2017. Achim Kopf, The enigmatic consolidation of diatomaceous sediment, Marine Geology, Volume 385,173-184, ISSN 0025-3227, https://doi.org/10.1016/j.margeo.2017.01.006.

Wu, W., Cong, S., 2020. Silica and diatomite fillers modified fluorine rubber composites treated by silane-coupling agents. J. Vinyl Add. Technol. https://doi.org/10.1002/vnl.21715.

You, Y., Jin, G., Pan, Z., Guo, R.-M.-P.-C.-E., 2021. Method for Space-Filling Design in Constrained Space with Multiple Types of Factors. Mathematics 9, 3314. https://doi.org/10.3390/math9243314.

Yun, Q., Ge, Y., Chen, B., Li, L., Wa, Q., Long, H., Zhang, H., 2022. Hybridization of 2D Nanomaterials with 3D Graphene Architectures for Electrochemical Energy Storage and Conversion. Adv. Funct. Mater. 2202319. https://doi.org/10.1002/adfm.202202319.

Zahajská, P., Opfergelt, S., Fritz, S.C., Stadmark, J., Conley, D.J., 2020. what is diatomite. Quat. Res. 96, 48–52.

Zhang, Y., Cai, R., Wang, D., Li, K., Sun, Q., Xiao, Y., Teng, H., Huang, X., Sun, T., Liu, Z., Yao, K., Zhang, Y., Yang, P., 2022. Lightweight, Low-Cost Co_2SiO_4@diatomite Core-Shell Composite Material for High-Efficiency Microwave Absorption. Molecules 27, 1055. https://doi.org/10.3390/molecules27031055.

Zhou, Y., Xi, W., Xie, Z., You, Z., Jiang, X., Han, B., Lang, R., Wu, C., 2021. 2021, High-Loading Pt Single-Atom Catalyst on CeO2. Modified Diatomite Support. Chem Asian J. 16 (18), 2622–2625. https://doi.org/10.1002/asia.202100730. Epub. PMID: 34403212.